

# NVH Analysis and Simulation of Automotive E-Axles

D. Marano, L. Pascale, J. Langhart, S. Ebrahimi, T. Giese

## Introduction

The automotive industry is continuously developing new electrified powertrain architectures and vehicle technologies to optimize vehicle fuel consumption and reduce carbon dioxide (CO<sub>2</sub>) and other pollutant emissions to withstand the regulations. According to the European Community (EU) statistics (Ref. 1) transportation accounts for 20% of total energy use and is responsible for around 25% of the total EU emissions of carbon dioxide, the main greenhouse gas. The European regulation 2019/631 has set a new EU fleet-wide CO<sub>2</sub> emission targets, as a percentage reduction starting from 2021 points: 15% reduction from 2025 on and 37.5% from 2030 on. In the USA, transportation accounts for 28% of total energy use and is responsible for 33% of total CO<sub>2</sub> emission. The USA national program for greenhouse gas emissions (GHG) and fuel economy standards for light-duty vehicles (passenger cars and trucks) was developed jointly by EPA and the National Highway Traffic Safety Administration (NHTSA). NHTSA and the EPA are proposing the “Safer Affordable Fuel-Efficient (SAFE) Vehicles Rule for Model Years 2021–2026 Passenger Cars and Light Trucks” (Ref. 1). The SAFE Vehicles Rule, if finalized, will establish new standards for Corporate Average Fuel Economy (CAFE) and tailpipe Green House Gas (GHG) emission standards for passenger cars and light trucks covering model years 2021 through 2026.

Some of the main drivers of powertrain electrification are the improved efficiency of the architectures, the displacement of fossil fuel as a primary energy source, the reduced impact on the environment (at the site of utilization), and the reduced cost of fueling. The electrified vehicles architectures actually on the market can be divided in Hybrid Electric Vehicles (HEV), Plug-In Hybrid Electric Vehicles (PHEV), Battery Electric Vehicle (BEV, AEV) and Fuel Cell Electric Vehicles (FCEV).

The HEV (hybrid electric vehicle) vehicle carries both an internal combustion and an electric propulsion system: for space and weight reasons, the latter uses a small battery; generally, both are capable of moving the car.

The PHEV (plug-in hybrid electric vehicle) configuration has almost universally replaced the HEV layout from which it derives, enhancing its charging capabilities via a grid connection, typically only in AC.

In the BEV (battery electric vehicle) architecture, electric energy enters the vehicle as alternate current (going through an AC/DC converter) or direct current according to the type of charger. From here it goes through an inverter to be fed to the electric motor, typically AC synchronous. Wheels are also connected to a generator for the recuperation of braking energy.

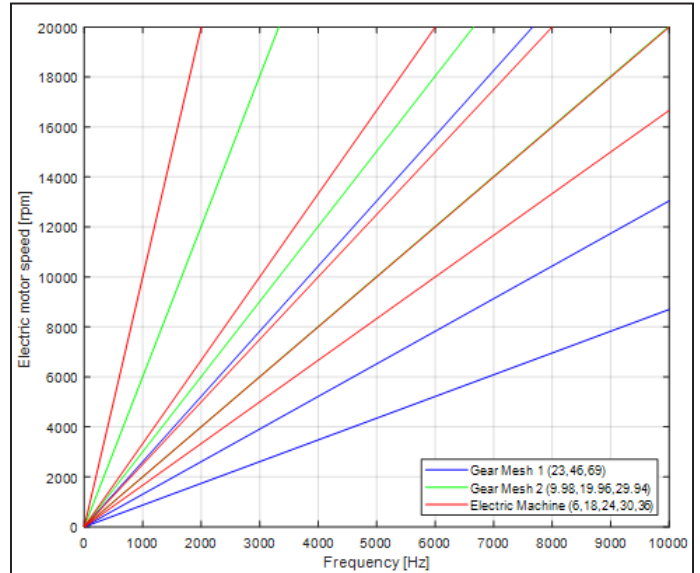


Figure 1 Campbell plot of the case study transmission.

The FCEV (fuel cell electric vehicles) vehicle has an electric propulsion system with the electric energy coming from the fuel cell stack where hydrogen is oxidized; such energy can be fed either directly to the electric motor or to the small battery.

The change from conventional vehicles to vehicles propelled by Electric Drive Units (EDUs) leads to a reduction in overall vehicle exterior and interior noise levels, especially during low-speed vehicle operation. Even though the radiated sound power of EV is lower than internal combustion engine (ICE) powered vehicles, the NVH behavior of such vehicles can be objectionable due to the presence of tonal noise coming from electric machines and gear train components as well as the high-frequency noise generated by the DC/AC converters. Advanced simulation of the EDU’s NVH behavior in the design phase is thus critical to fulfill the vehicle NVH integration process and reduce the time to market (TTM).

Two target setting approaches for transmission and electric motor NVH are presented in (Ref. 2): the “vehicle-centric” synthesis of component level noise data to the vehicle interior (using specific or generic transfer function data) and the “component level” definition of noise targets, allowing efficient assessment of component NVH performance. Various aspects of the EDU NVH development process are qualitatively described in (Ref. 3) and the areas to be addressed during the development for optimized NVH behavior are identified concerning geartrain, electric motor, and power electronics; a state of the art regarding these topics is performed in the following.

The theory regarding the fundamentals of geartrain NVH optimization is well explained in the books of Smith (Ref. 4) and Beranek (Ref. 5). An effective literature survey of gear noise and vibration has been conducted by Akerblom (Ref. 6), concerning gear noise excitation, dynamic models, and gear noise and vibration measurement. Several studies on the nonlinear dynamics of gear transmissions, both spur, and planetary, have been conducted worldwide by research institutes such as the Gear Lab at Ohio State University (Refs. 7–10), the “Gear Research center (FZG)” at Technical University of Munich (Refs. 11–14), and Powertrain Laboratory at University of Modena and Reggio Emilia (Refs. 15–18).

The electric motor (EM) and power electronics NVH performance is a key consideration in the design of EDUs. The high-frequency noise generated by the electromagnetic force of EM and the high-frequency umbrella shape noise of DC/AD converters is subjectively quite annoying, thus many OEMs and research institutes have addressed the problem. The fundamental concepts to improve the noise performance of electrical motors at the design stage are explained in (Ref. 19). Kang has analyzed the electromagnetic noise of an EM in a pure electric car (Ref. 20), providing an effective state of the art.

This paper addresses a methodology for NVH analysis and simulation of an automotive E-axle. The theoretical calculation of a Campbell diagram including electrical and mechanical orders is presented and a constrained modal analysis of the system on mountings is performed to calculate its natural frequencies.

The electric axle is modeled as a fully flexible multibody system after having applied the Craig-Bampton modal reduction technique, whose details are discussed in this paper, to all bodies. The forced response is calculated at a constant speed of the electric motor. NVH performance of high-contact ratio gears (HCR) is evaluated with respect to standard ISO-53 gear profile A. For this purpose, peak-to-peak transmission error (PPTE), gear meshing, and bearing forces are compared for both configurations. The effect of the housing stiffness is investigated.

Housing equivalent radiated power (ERP) resulting from both ISO-53 profile A and HCR gears simulation is compared showing the reduction of surface normal velocities. The critical areas for the design of the housing are shown by means of contour plots.

## E-Axle Noise and Vibration Analysis

**Campbell diagram of a mechanical transmission.** The Campbell diagram represents the vibration frequencies of a system at various operating speeds. A typical Campbell diagram plot is shown (Fig. 1): the system frequency is along the X-axis and the electric motor speed is along the Y-axis. This study is necessary to determine if a natural frequency is excited by running frequency or its harmonics and if orders coming from different sources overlap, which must be avoided. In the following, calculation of the excitation frequencies (also called excitation orders) of both electrical and mechanical components is presented.

**Shaft unbalance and misalignment excitation orders.** All rotating machines produce vibrations that typically arise from the system dynamics faults such as shaft misalignment and rotor unbalance. The ISO 1940 (Ref. 21) defines unbalance as: “that condition, which exists in a rotor when vibratory, force or motion

is imparted to its bearings as a result of centrifugal forces,” and gives specifications for balance tolerances, and methods for verifying the residual unbalance.

For all types of unbalance, the FFT spectrum will show a predominant  $1 \times \text{rpm}$  frequency of vibration, or equivalently, an excitation order equal to 1. The vibration force produced by an unbalance mass  $M_u$  is represented by:

$$F_u = M_u \cdot r \cdot \omega^2 \sin(\omega t) \quad (1)$$

where time  $t$  is in seconds. The vibration amplitude at the  $1 \times \text{rpm}$  frequency varies proportionally to the square of the rotational speed.

Shaft misalignment, as unbalance, is a major cause of machinery vibration. There are two types of misalignment: parallel and angular misalignment. With parallel misalignment, the shaft centerlines are parallel, but they have an offset; with angular misalignment, the shaft centerline meets at an angle with each other. As explained in (Ref. 22), angular misalignment results in axial vibrations at the  $1 \times \text{rpm}$  and  $2 \times \text{rpm}$  frequency; parallel misalignment results in a  $2 \times \text{rpm}$  vibration in the radial direction that approaches a  $180^\circ$  phase difference across the coupling. When either angular or parallel misalignment is severe, it can generate high-amplitude peaks at higher harmonics ( $3 \times$  to  $8 \times$ ).

**Gear excitation orders.** The spectrum of any electric axle shows a range of frequencies related to gear mesh frequency (GMF). The fundamental gear mesh frequency  $f_m$  is calculated as the product of the number of teeth of a pinion  $z_1$  (or a gear  $z_2$ ), and its respective shaft frequency  $f_{s1}$  ( $f_{s2}$ ):

$$f_m = z \cdot f_s \quad (2)$$

The amplitude of the gear meshing frequency is usually related to the transmitted load, thus vibration analysis of the e-axle should be conducted at the maximum power. Sidebands

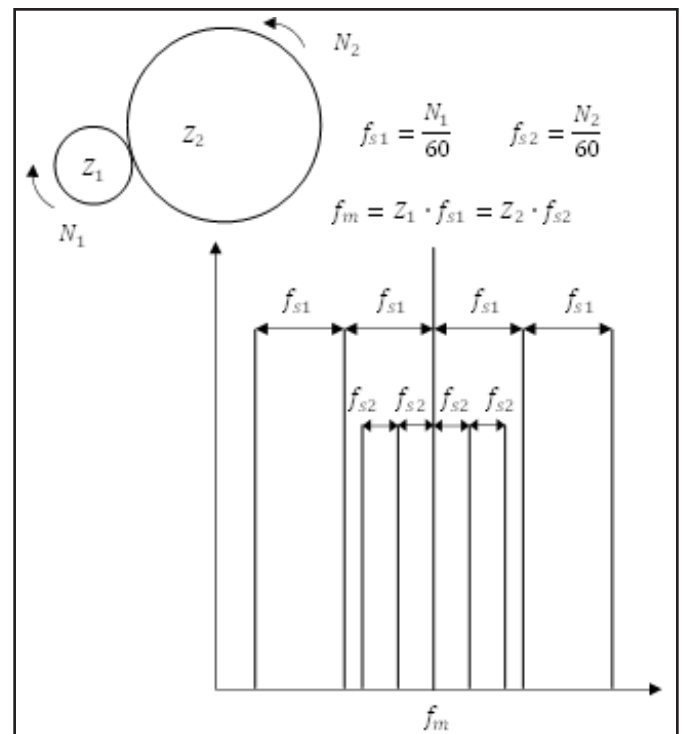


Figure 2 Gear mesh frequency.

around the gear mesh frequency, having a frequency  $f_m \pm$  the shafts rotational frequencies  $f_{s1}, f_{s2}$  and its harmonics are quite common due to gear faults such as wear, defects, misalignment, and eccentricity. A description of sidebands related to gearing defects is presented in (Ref. 22).

In automotive e-axes, epicyclic gearboxes are often used due to the high-power density. In epicyclic systems, planet gears are mounted on a movable carrier revolving about a central gear with a fixed axis (Fig. 3). For the simple case where the sun gear represents the input and the carrier the output, with the ring gear fixed, the fundamental mesh frequency is calculated as:

$$f_m = z_r \cdot \frac{n_c}{60} = \frac{z_r \cdot z_s}{z_r + z_s} \cdot \frac{n_s}{60} \quad (3)$$

Where  $z_r$  and  $z_s$  are, respectively, the ring gear and sun gear number of teeth,  $n_c$  and  $n_s$  are respectively the carrier and the sun shaft rotational speeds.

An analysis of sidebands for epicyclic gearbox can be found, e.g., in (Refs. 23–24). Different combinations of input/output or more complex schemes are described in ANSI/AGMA 6123-C16 (Ref. 25).

**Bearings excitation orders.** The vibrations related to the bearings can be either tonal or broadband. Tonal vibrations in new bearings are generally caused by production imperfections (Ref. 23), including, but not limited to, the cases when the stiffness of both inner and outer rings is not ideal and they get ovalized due to the clamping for grinding. Broadband vibrations originate from the defects of raceways and rolling elements imperfections; a smooth operation is thus expected when bearings are new. The SKF company has published a comprehensive analysis of bearing damage and failure modes (Ref. 26), and a

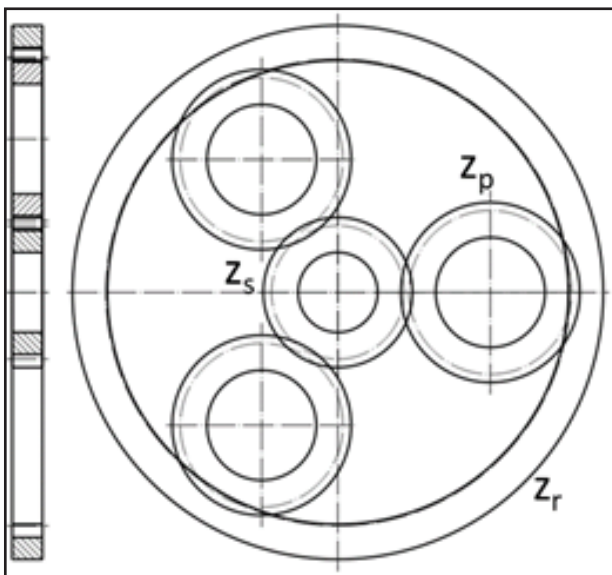


Figure 3 An epicyclic gearbox.

Table 1 Bearing geometric parameters	
Outer diameter	$D_1$
Bore diameter	$D_2$
Pitch diameter	$PD \approx \frac{D_1 + D_2}{2}$
Rolling element diameter	$D_b$
Contact angle	$\beta$
Number of rolling elements	$n$
Revolutions per second (or relative speed difference between outer and inner race)	$rps$

guide to the interpretation of vibration signals (Refs. 27–28). In the following, calculation of the main bearing defect frequencies is presented as a function of the ball bearing dimensions and other bearings’ geometric parameters (Table 1).

**Fundamental train frequency (FTF)**

The fundamental train frequency is related to defects affecting the rotation of the cage; the rotational frequency of the bearing cage may be calculated as:

$$f_{FTF} = \frac{rps}{2} \cdot \left(1 - \frac{D_b}{PD} \cdot \cos \beta\right) \quad (4)$$

**Ball pass frequency of the outer race (BPFO)**

The ball pass frequency of the outer race is the frequency of the rolling elements passing by a defect located on the outer race-way; it can be calculated as:

$$f_{BPFO} = \frac{n \cdot rps}{2} \cdot \left(1 - \frac{D_b}{PD} \cdot \cos \beta\right) \quad (5)$$

**Ball pass frequency of the inner race (BPFII)**

The ball pass frequency of the inner race is the frequency of the rolling elements passing by a defect located on the inner race-way; it can be calculated as:

$$f_{BPFII} = \frac{n \cdot rps}{2} \cdot \left(1 + \frac{D_b}{PD} \cdot \cos \beta\right) \quad (6)$$

**Ball-spin/roller frequency (BSF)**

The ball-spin/roller frequency is the frequency related to the impacts of the rolling element with either the inner or the outer race; it can be calculated as:

$$f_{BSF} = \frac{n \cdot rps}{2 \cdot D_b} \cdot \left[1 - \left(\frac{D_b}{PD} \cdot \cos \beta\right)^2\right] \quad (7)$$

**Electric machine excitation orders.** The noise of an electric motor is caused by the electromagnetic force in the air gap, exciting the stator and the motor casing. The electromagnetic force can be decomposed in a tangential force, generating the e-motor torque, and a radial force responsible for the e-motor noise which does not affect the operation of the e-motor. The electromagnetic excitation force is influenced by the design parameters of the electric motor, such as the motor topology (number of poles and slots), the shape of the poles and slots, the shape of the current, and several other parameters. Based on the theoretical calculation formulas reported in (Ref. 20), the frequency characteristics and spatial order characteristics of the electromagnetic radial force of a permanent magnet synchronous motor are obtained (Ref. 29). Table 2 lists the main electromagnetic frequencies  $f_m$ , where  $p$  is the number of pole pairs,  $s$  is the number of stator slots,  $f$  is the motor rotational frequency in Hz,  $k=0,1,2,3,\dots, k_1=0,1,2,3,\dots, n=6k \pm 1$ ).

**Excitation orders of the case study e-axle.** The electric axle

Table 2 Main electric motor frequencies of radial force wave in synchronous motors	
Product of the stator spatial harmonics of the same number	$f_1 = 2pnf$
Product of the rotor spatial harmonics of the same number	$f_2 = 2pn(1 \pm 2k_1) f$
Product of the stator winding and rotor spatial harmonics	$f_3 = 2pn(1 + k_1) f$ and $f_3 = 2pnk_1 f$
Interaction of the rotor magnetic field and the slotted core of the stator	$f_4 = p\mu_n f$ where $\mu_n = \text{int} \left[ \frac{ks}{p} \right]$

Gear Parameters		I stage		II stage	
		Gear 1	Gear 2	Gear 3	Gear 4
Number of teeth	$z$ [-]	23	53	23	89
Helix angle at reference circle	$\beta$ [°]	30		15	
Normal pressure angle	$\alpha_n$ [°]	20		20	
Normal module	$mn$ [mm]	2.5		2.6	
Profile shift coefficient	$x^*$ [-]	0.0163	-0.6682	0.4706	-0.6659
Face width	$b$ [mm]	25	23	40	38
Center distance	$a$ [mm]	107.99		150.22	
Gear Mesh Excitation order	$GMF$	23.00		9.98	
Gear profile LCR	$h_{ref}^* \rho_{ref}^* / h_a^*$	1.25/0.38/1.00	1.25/0.38/1.00	1.25/0.38/1.00	1.25/0.38/1.00
Gear profile HCR	$h_{ref}^* \rho_{ref}^* / h_a^*$	1.80/0.19/1.35	1.60/0.29/1.60	1.60/0.29/1.35	1.60/0.29/1.45
Transverse contact ratio LCR	$\epsilon_a$ [-]	1.43		1.53	
Transverse contact ratio HCR		2.05		2.10	
Overlap ratio	$\epsilon_\beta$ [-]	1.46		1.20	

Bearing	Type	$D_1$ [mm]	$D_2$ [mm]	$n$ [mm]	$PD$ [mm]	$D_b$ [mm]	$n$ [-]	$\beta$ [°]	FTF	BPFO	BPFI	BSF
b1 – EM rotor	Ball Bearing	50	90	20	70.00	12.7	10	0	0.41	4.09	5.91	2.67
b2 – EM rotor	Ball Bearing	50	110	27	80.00	19.1	8	0	0.38	3.05	4.95	1.98
B1 – Input (EM side)	Ball Bearing	45	85	19	65.00	12.3	10	0	0.41	4.05	5.95	2.55
B2 – Input	Ball Bearing	45	85	19	65.00	12.3	10	0	0.41	4.05	5.95	2.55
B3 – Intermediate	Ball Bearing	50	90	20	70.00	12.7	10	0	0.18	1.77	2.55	1.15
B4 – Intermediate	Ball Bearing	50	90	20	70.00	12.7	10	0	0.18	1.77	2.55	1.15
B5 – Output	Taper roller bearing	80	110	20	94.67	7.4	34	NA	-	-	-	-
B6 – Output	Taper roller bearing	80	110	20	94.67	7.4	34	NA	-	-	-	-

analyzed in the following is a single-speed, two-stage gearbox powering the front wheels of an electric vehicle (Fig. 4).

Power is supplied by a permanent magnet synchronous motor to the input shaft, through a spline connection. The electric machine has  $2p=6$  poles and  $s=36$  stator slots. The output gear stage is integral to the differential case. The modeling of the differential stage is not considered in the present paper.

Table 3 reports gears macrogeometry data for two designs—low-contact ratio (LCR) gears and high-contact ratio (HCR) gears—with a transverse contact ratio  $\epsilon_a > 2$ . For both designs, first-stage gear mesh order is 23.00 and the second-stage gear mesh order is 9.98; order 1 is referred to electric machine shaft.

Table 4 shows bearings selection for the electric axle, and main excitation orders. For the bearings of the intermediate and output shafts, calculated orders are divided by 53/23 and 53/2389/23 respectively, in order to report them to the electric machine.

In Table 5 main calculated electric machine orders are reported. A practical design rule is to avoid overlapping multiples of the number of poles with gear mesh orders (distance

Product of the stator spatial harmonics of the same number	6, 30, 42, ...
Product of the rotor spatial harmonics of the same number	6, 18, 30, 42, ...
Product of the stator winding and rotor spatial harmonics	6, 12, 18, 24, 30, 36, 42, ...
Interaction of the rotor magnetic field and the slotted core of the stator	36, 72, ...

between orders should be at least 3%). On the case study electric axle, however, electric machine order 24 is very close to the first-stage gear mesh order, 23, and the third harmonic of the second-stage gear mesh order, 9.98, matches the electric machine order 30 (Fig. 1).

**Multibody simulation approach.** Dynamic response of the electric axle to the inputs such as electric machine torque (mean and ripple torque), presence of unbalanced forces, misalignments etc. has to be evaluated in order to predict the displacement and acceleration levels on the housing and noise emission.

- To this purpose, multibody tools are adopted where each body is representative of a certain substructure. Considering the case of an electric axle, one might consider the following bodies:
- Housing with its supports, the outer cages of bearings, the stator of the electric machine
- Rotor of the electric machine
- Each rotating shaft with gears and inner cages of supporting bearings

Then, connections between bodies through joints must be set up. General joints (force-displacement and force-velocity laws) can be used to model spline connections and the presence of mountings; specific joints should be adopted to model gears (shaft-shaft) and bearings (shaft-housing) connections.

According to multi-body theory, the displacement field of each substructure is described with a linear combination of suitable shape functions (i.e. — modes). The size of the numerical problem can be significantly reduced if only shape functions related to the

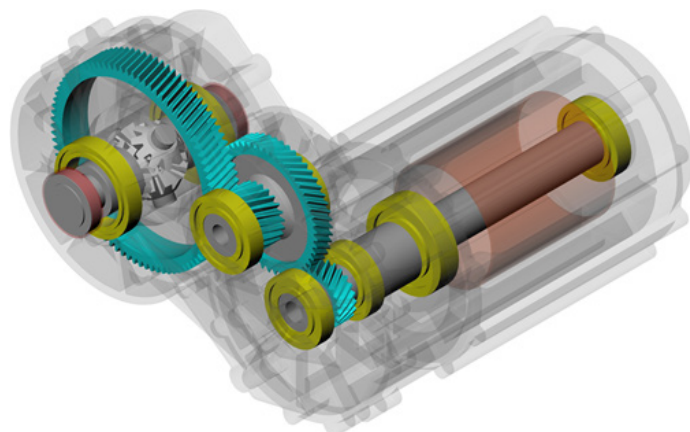


**Figure 4 E-axle layout in KISSsys.**

frequency range of interest are considered (Ref. 30).

**Modal analysis.** Modal analysis is the process of determining the dynamic characteristics of a system in forms of natural frequencies, damping factors, and mode shapes and using them to formulate a mathematical model to describe its dynamic behavior (Ref. 31). Free vibrations of an MDOF  $\{x\}$  system can be studied, starting from its undamped equation of motion:

$$[M]\{\ddot{x}\}+[K]\{x\}=\{0\} \quad (8)$$

where  $\{r\}$  is the mass matrix, usually positive definite, is the stiffness matrix which is semi-positive definite in case the system shows rigid body modes (as in the case of an electric axle on its mountings). The non-trivial solution of Equation 8 provides the free vibration of the system. Imposing a type of motion for which all Lagrangian coordinates depend on the same time function, i.e.  $\{x\}=\{\phi\} \sin(\omega t)$ , leads to:

$$(-\omega^2[M]\{\ddot{x}\}+[K])\{\phi\}=\{0\} \quad (9)$$

Non-trivial solutions are those for which the matrix  $(-\omega^2[M]+[K])$  is singular:

$$\det(-\omega^2[M]\{\ddot{x}\}+[K])=\{0\} \quad (10)$$

Equation 10 represents an Eigenvalue problem, where  $\omega^2$  is the Eigenvalue (the square of the natural frequency of the system) and  $\{\phi\}$  is the Eigenvector (the mode shape).

Electric axles are supported by mountings, whose main purpose is to isolate the disturbance coming from the system itself from the vehicle structure. To determine the six low-frequency rigid modes the mass matrix assumes the following form:

$$[M]=\begin{bmatrix} m & 0 & 0 & 0 & 0 & 0 \\ 0 & m & 0 & 0 & 0 & 0 \\ 0 & 0 & m & 0 & 0 & 0 \\ 0 & 0 & 0 & J_{xx} & -J_{xy} & -J_{xz} \\ 0 & 0 & 0 & -J_{yx} & J_{yy} & -J_{yz} \\ 0 & 0 & 0 & -J_{zx} & -J_{zy} & J_{zz} \end{bmatrix} \quad (11)$$

where  $m$  is the total mass of the system and  $J_{ij}$  represents the components of the mass moment of inertia tensor around each axis. The stiffness matrix depends on mountings characteristics in terms of static and dynamic stiffness (Ref. 32).

The first flexible modes usually encountered for an electric axle are related to the bending modes of the supports which connect the housing to the mountings. These modes can lead to NVH disturbances for the driver if they propagate towards the vehicle structure interacting with other dynamic systems in a certain frequency band; i.e. — in a certain range of vehicle speed.

To overcome issues of this type, it might be necessary to increase the supports stiffness-to-mass ratio corresponding to the disturbing mode to exit the interest frequency band or to reduce vibration; for example, by utilizing a tuned mass damper.

Other potential sources of noise are membrane modes of the housing or of other components mounted on it, such as the inverter. So, in the design phase, apart from strength calculation also modal characteristics of the system must be considered in order to avoid NVH issues.

**Modal reduction techniques.** In structural dynamics, finite element models are adopted to represent the dynamic behavior of a substructure. These models are often too refined and have millions of DOFs, therefore solving dynamic problems may result in unfeasible computation times. Thus, component model reduction methods are adopted, whose idea is modal

superposition, i.e. — nodal displacements are written as a linear combination of normal modes  $\{\phi_j\}$  and modal amplitudes  $\eta_j$ :

$$\{x\}=\sum_{j=1}^n\{\phi_j\}\eta_j \quad (12)$$

The general form of the equations of motion for each substructure reads:

$$[M]\{\ddot{x}\}+[C]\{\dot{x}\}+[K]\{x\}=\{p\}+\{g\} \quad (13)$$

where  $[M]$  is the substructure mass matrix,  $[C]$  is the damping matrix,  $[K]$  is the stiffness matrix and  $\{p\}+\{g\}$  is the force vector;  $\{p\}$  denotes the externally applied forces and  $\{g\}$  the forces coming from the neighboring substructures. The reduction is performed transforming the set of original DOFs  $\{x\}$  into a set of generalized DOFs  $\{q\}$  via the transformation matrix  $[R]$ :

$$\{x\}=[R]\{q\} \quad (14)$$

$[R]$  is the reduction basis, whose dimensions are  $n \times r$ . The reduced set of DOFs ( $r$ ) should be small with respect to the original set of DOFs ( $n$ ), for an efficient reduction.

Substituting Equation (14) into Equation (13) leads to:

$$[M][R]\{\ddot{q}\}+[C][R]\{\dot{q}\}+[K][R]\{q\}=\{p\}+\{g\}+\{r\} \quad (15)$$

where  $\{r\}$  is the error arising from the fact that the reduced set of DOFs does not span the full solution space. An error is only allowed in the space not spanned by the reduction basis, i.e.  $[R]^T\{r\}=\{0\}$ . The projection of Equation (15) onto the reduction basis gives:

$$[R]^T[M][R]\{\ddot{q}\}+[R]^T[C][R]\{\dot{q}\}+[R]^T[K][R]\{q\}=[R]^T\{p\}+[R]^T\{g\} \quad (16)$$

i.e.:

$$[\tilde{M}]\{\ddot{q}\}+[\tilde{C}]\{\dot{q}\}+[\tilde{K}]\{q\}=\{\tilde{p}\}+\{\tilde{g}\} \quad (17)$$

Generally, a basis is built from a set of vibration modes, which contain information of the substructure's dynamic behavior, and a set of static modes, which represent the static deformation caused by neighboring substructures (Ref. 33).

**The Craig-Bampton method.** In the Craig-Bampton method (Ref. 34) the substructure DOFs are divided into boundary and interface DOFs, each of them referring to a specific node-set in the finite element model:

The vibrational information is the set of fixed-interface vibration modes; the substructure is fixed at its boundary DOFs and analysis is done to obtain the Eigenmodes.

Constraint modes are used to represent the static deformation of a substructure caused by neighboring substructures.

*Fixed-interface* vibration modes can be computed by constraining the boundary DOFs. The first step is the partitioning of DOFs into the boundary  $\{x_b\}$  and internal  $\{x_i\}$ . By neglecting the damping, Equation (13) can be written as:

$$\begin{bmatrix} [M_{bb}] & [M_{bi}] \\ [M_{ib}] & [M_{ii}] \end{bmatrix} \begin{Bmatrix} \{\ddot{x}_b\} \\ \{\ddot{x}_i\} \end{Bmatrix} + \begin{bmatrix} [K_{bb}] & [K_{bi}] \\ [K_{ib}] & [K_{ii}] \end{bmatrix} \begin{Bmatrix} \{x_b\} \\ \{x_i\} \end{Bmatrix} + \begin{Bmatrix} \{g_b\} \\ \{0\} \end{Bmatrix} = \begin{Bmatrix} \{p_b\} \\ \{0\} \end{Bmatrix} \quad (18)$$

where  $\{g_b\}$  contains the reaction forces with neighboring substructures. Constraining the boundary DOFs ( $\{x_b\}=\{0\}$ ) leads to:

$$[M_{ii}]\{\ddot{x}_i\}+[K_{ii}]\{x_i\}=\{0\} \quad (19)$$

That can be solved as an Eigenvalue problem:

$$(-\omega_{ij}^2[M_{ii}]+[K_{ii}])\{\phi_{ij}\}=\{0\} \quad (20)$$

The result is the set of Eigenmodes and Eigenfrequencies of the substructure constrained at its boundary DOFs (fixed-interface vibration modes):

$$\{x_i\}=[\phi_i]\{\eta_i\} \quad (21)$$

Constraint modes contain the substructure static response to an applied boundary displacement. They are in fact representative of the static deformation due to a unit displacement applied to one of the boundary DOFs, while the remaining boundary DOFs are restrained, and no forces are applied to the internal DOFs.

The first step is again partitioning of the DOFs into the boundary and internal, which leads to Equation (18). The second equation, neglecting the inertia forces, reads:

$$[K_{ib}]\{x_b\} + [K_{ii}]\{x_i\} = \{0\} \quad (22)$$

From which:

$$\{x_i\} = -[K_{ii}]^{-1}[K_{ib}]\{x_b\} \quad (23)$$

The columns of the static condensation matrix  $-[K_{ii}]^{-1}[K_{ib}]$  contain the static modes, which represent the static response of the internal DOFs  $\{x_i\}$  for a unit displacement of the boundary DOFs  $\{x_b\}$ .

The original set of DOFs can thus be reduced to a set of boundary DOFs, as:

$$\begin{Bmatrix} x_b \\ x_i \end{Bmatrix} = \begin{bmatrix} [I] \\ -[K_{ii}]^{-1}[K_{ib}] \end{bmatrix} \{x_b\} = \begin{bmatrix} [I] \\ [\psi_{C,i}] \end{bmatrix} \{x_b\} = [\psi_C] \{x_b\} \quad (24)$$

Once constraint modes and fixed-interface vibration modes have been obtained, the displacement field  $\{x_b\}$  of the interface nodes can be written through the superposition of the static and dynamic modes, and it is a function of the displacement field of the boundary nodes only; this is a crucial point of every condensation method:

$$\{x_i\} = [\psi_{C,i}]\{x_b\} + [\phi_i]\{\eta_i\} \quad (25)$$

The reduction basis therefore yields:

$$\begin{Bmatrix} x_b \\ x_i \end{Bmatrix} = \begin{Bmatrix} \{x_b\} \\ [\psi_{C,i}]\{x_b\} + [\phi_i]\{\eta_i\} \end{Bmatrix} = \begin{bmatrix} [I] & [0] \\ [\psi_{C,i}] & [\phi_i] \end{bmatrix} \begin{Bmatrix} \{x_b\} \\ \{\eta_i\} \end{Bmatrix} = [R_{CB}] \begin{Bmatrix} \{x_b\} \\ \{\eta_i\} \end{Bmatrix} \quad (26)$$

Finally,  $[\tilde{M}] = [R_{CB}]^T [M] [R_{CB}]$  and  $[\tilde{K}] = [R_{CB}]^T [K] [R_{CB}]$ .

The generalized DOFs vector contains both physical displacements of the boundary nodes  $\{x_b\}$  and modal coordinates  $\{\eta_i\}$ .

The first advantage of the Craig-Bampton method is the fact that both the constraint modes and the fixed-interface vibration

Table 6 Microgeometry modifications for LCR gearset				
Microgeometry modifications [] - LCR	I stage		II stage	
	Gear 1	Gear 2	Gear 3	Gear 4
Flank crowning	10	-	3	-
Helix angle modification	-5	-	-3	-
Tip relief (Long)	15 ( $d_{Ca}=67.78$ mm)	15 ( $d_{Ca}=151.59$ mm)	15 ( $d_{Ca}=62.29$ mm)	12 ( $d_{Ca}=235.96$ mm)
Profile crowning	3	-	-	-
Pressure angle modification	-2	-	-4	-

Table 7 Microgeometry modifications for HCR gearset				
Microgeometry modifications [] - HCR	I stage		II stage	
	Gear 1	Gear 2	Gear 3	Gear 4
Flank crowning	8	-	10	-
Helix angle modification	-5	-	-2	-2
Tip relief (Long)	14 ( $d_{Ca}=67.02$ mm)	14 ( $d_{Ca}=150.60$ mm)	15 ( $d_{Ca}=62.75$ mm)	15 ( $d_{Ca}=238.50$ mm)
Profile crowning	-	-	-	-
Pressure angle modification	-	-	-5	-

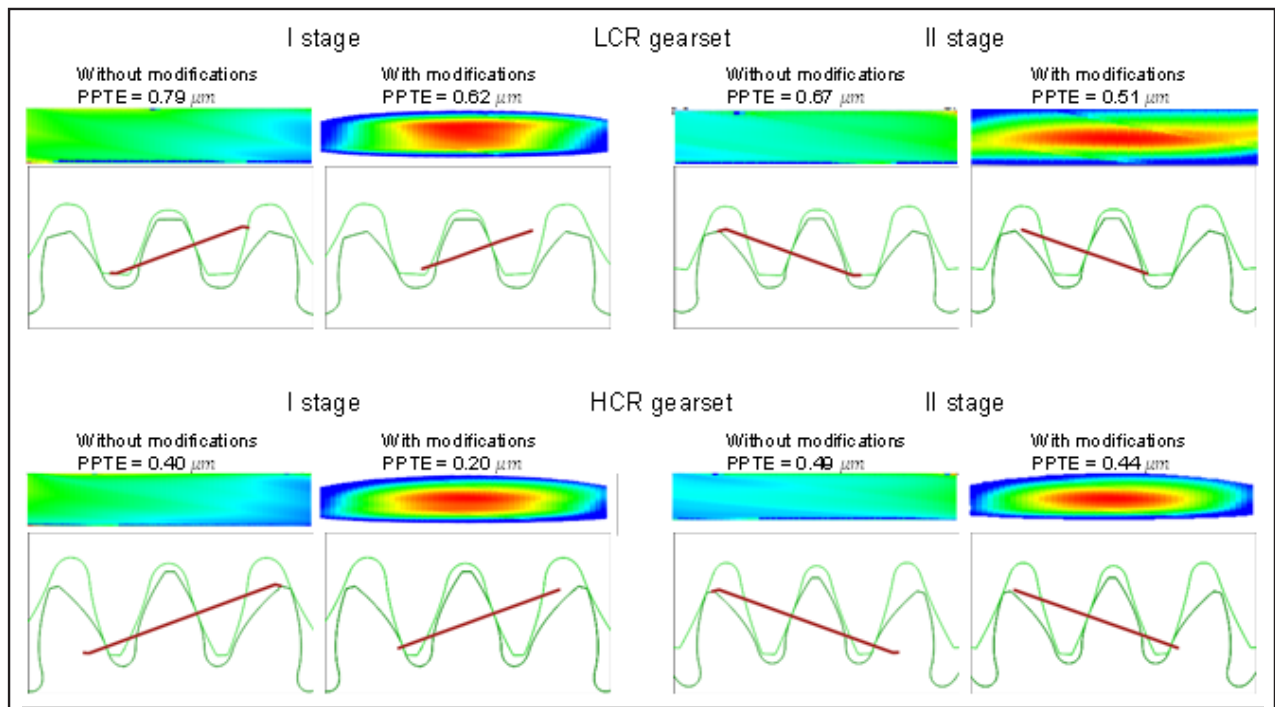


Figure 5 Effect of modifications on the contact pattern and static PPTE calculated in KISSsoft.

modes can be easily computed. Then, in the reduced system, the original boundary DOFs are retained, allowing to add or replace substructures without having to analyze again the full model. In fact, the system's substructures are connected with joints at the boundary nodes.

**E-axle noise and vibration simulation.** The simulations are carried out for performance improvement evaluation of the HCR gears with respect to the LCR gears regarding the peak-to-peak transmission error (PPTE), gear meshing, and bearing forces. Housing equivalent radiated power (ERP) resulting from HCR gear simulation is analyzed. Gear microgeometry modifications (Tables 1 and 2) have been designed with the help of *KISSsys*: helix angle modification and crowning have been adopted to reduce the face load factor  $K_{H\beta}$ , while tip relief and profile crowning have been adopted to eliminate contact shock and reduce the PPTE. Details on the methodology to design gear microgeometry are reported in (Ref. 35).

Table 8 E-axle modes of vibration			
Frequency [Hz]			
Mode 1	238	Mode 6	487
Mode 2	273	Mode 7	577
Mode 3	296	Mode 8	589
Mode 4	387	Mode 9	639
Mode 5	412	Mode 10	719

The following results are obtained for an input torque of 60 nm (nearly 50% of the rated torque) at 1,000 rpm.

**Constrained modal analysis.** Constrained modal analysis of the E-axle on its mountings has been performed to evaluate the system's natural frequencies. Firstly, ten eigenfrequencies are listed in Table 3.

The scope of this analysis is to predict the interaction of the main excitation orders with the system natural modes. In Figure 6, an extended Campbell diagram is shown, reporting the main excitation orders together with the system eigenfrequencies and the electric motor speed adopted for the multibody simulations (1,000 rpm). When these frequencies intersect the excitation orders, an amplification of the response is expected.

**Forced response analysis.** The forced response analysis is performed using *Recurdyn* a multi-body dynamics (MBD) software, importing gears data from a *KISSsys* model. Four simulations have been performed according to the following scheme:

1. LCR and HCR gearset, rigid housing
2. LCR and HCR gearset, flexible housing

**LCR and HCR gearset – rigid housing.** To better understand the effect of a higher transverse contact ratio on the dynamic transmission error and gear meshing force (thus on dynamic forces loading the bearings), the first simulation is carried out with rigid housing; the main excitation orders are as follows (Fig. 1):

- Orders 23 and 46: respectively, first and second harmonics of the gear mesh frequency for the first stage.
- Orders 10, 20 and 30: respectively, first, second and third harmonic of the gear mesh frequency for the second stage.

In Figure 7, the dynamic transmission error is plotted for both the gear stages. Furthermore, the harmonic spectrum of the

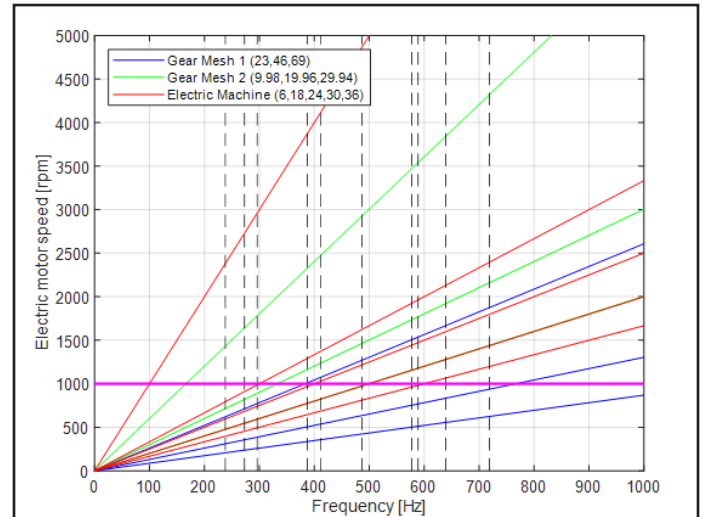


Figure 6 Extended Campbell plot including system Eigen frequencies and EM speed adopted for the multibody simulations.

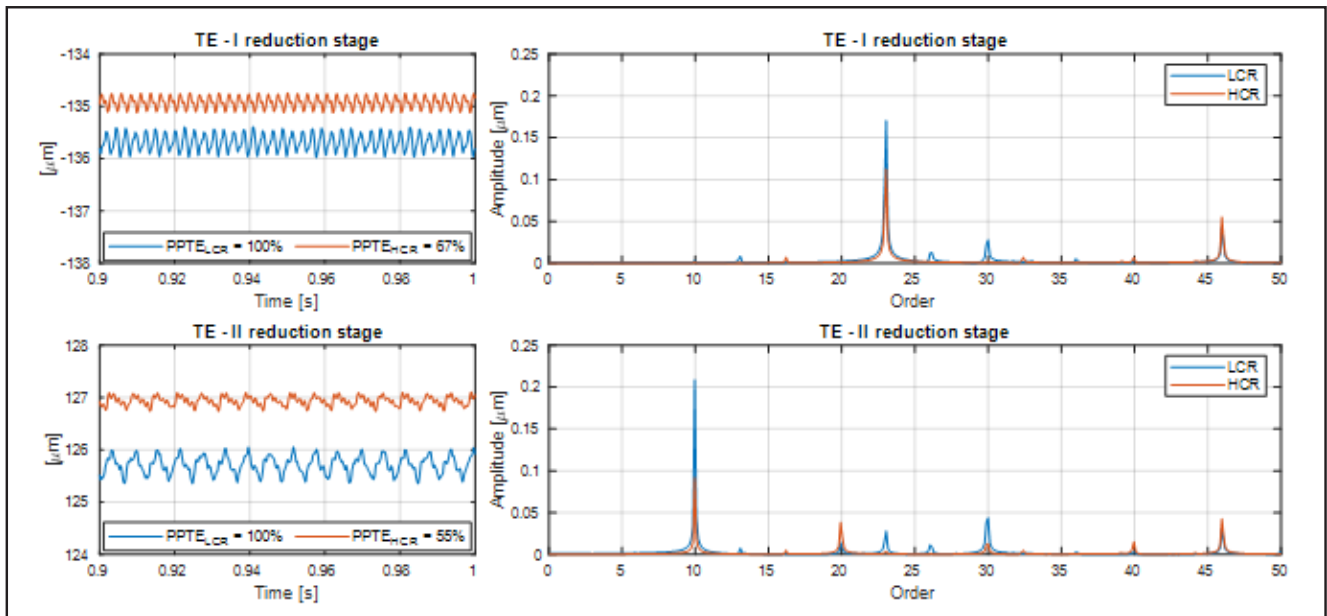
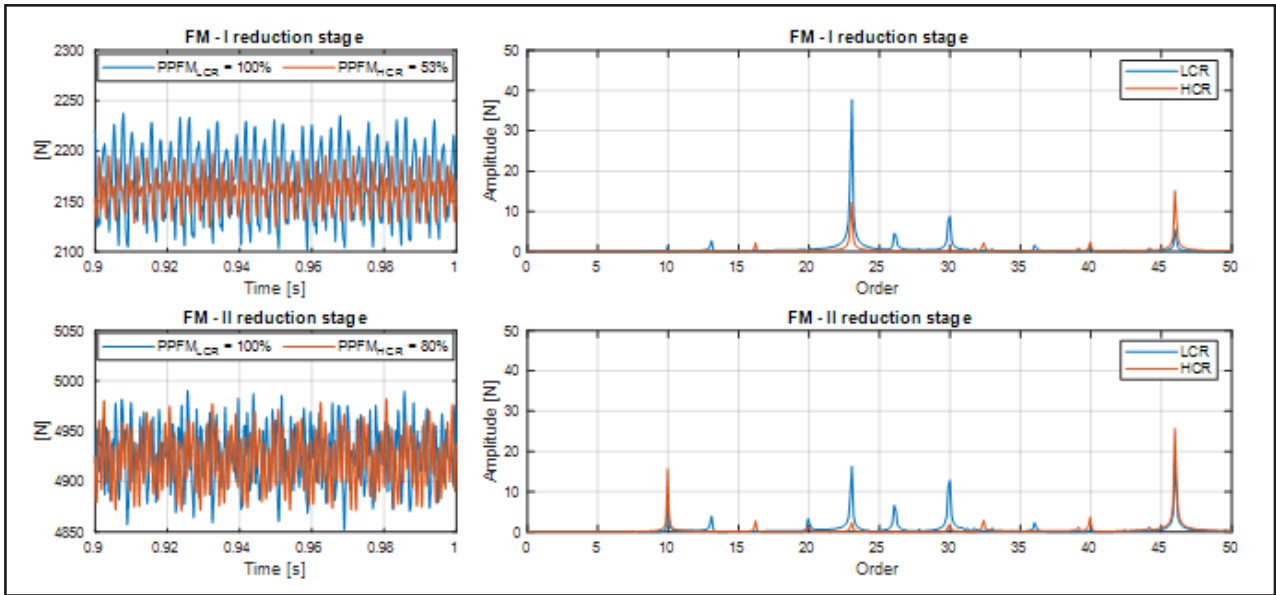


Figure 7 Transmission error and its harmonic content.



**Figure 8** Gear meshing force and its harmonic content.

signal is analyzed. Results confirm a significant reduction in the amplitudes of the meshing orders for both the first and second stages of the transmission.

In Figure 8, gear meshing forces are plotted and their harmonic content is analyzed. For the first drop, the dominant orders are the ones related to the gear meshing frequencies of the first reduction stage; for the second drop, apart from order 10 and its harmonics, the presence of order 23 is especially remarkable for the LCR gearset.

In Figure 10, transmission bearing forces are compared, and the signal spectrum is shown. Since the bearings transmit the dynamic load to the housing, a reduction of the harmonic content of the bearing forces leads to a reduction in the housing excitation, which eventually results in an overall noise level reduction; bearings are named according to Figure 9.

For all bearings, the force peak-to-peak has decreased, as well, most of the harmonics have been reduced by substituting the

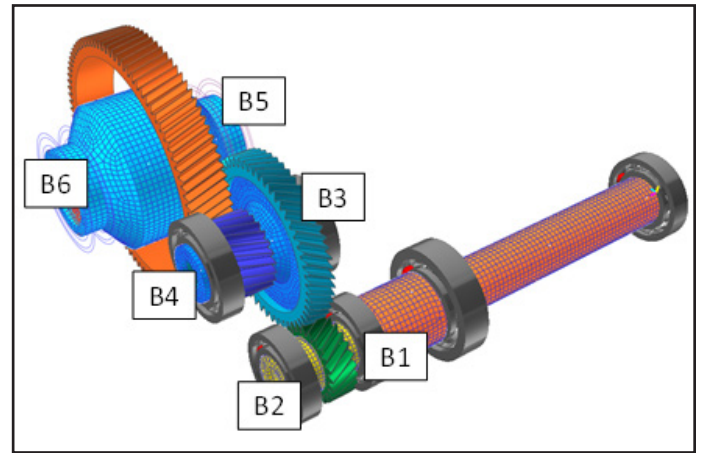


**Figure 9** Transmission bearings layout in Recurdyn.

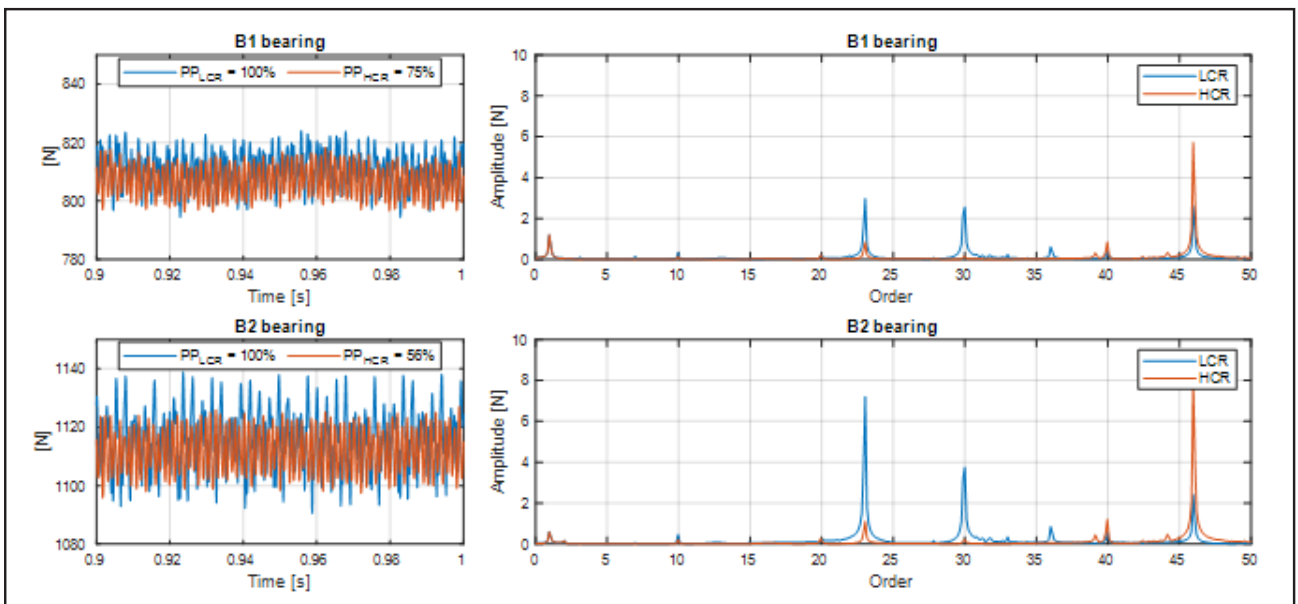


**Figure 10** Bearings forces FM.

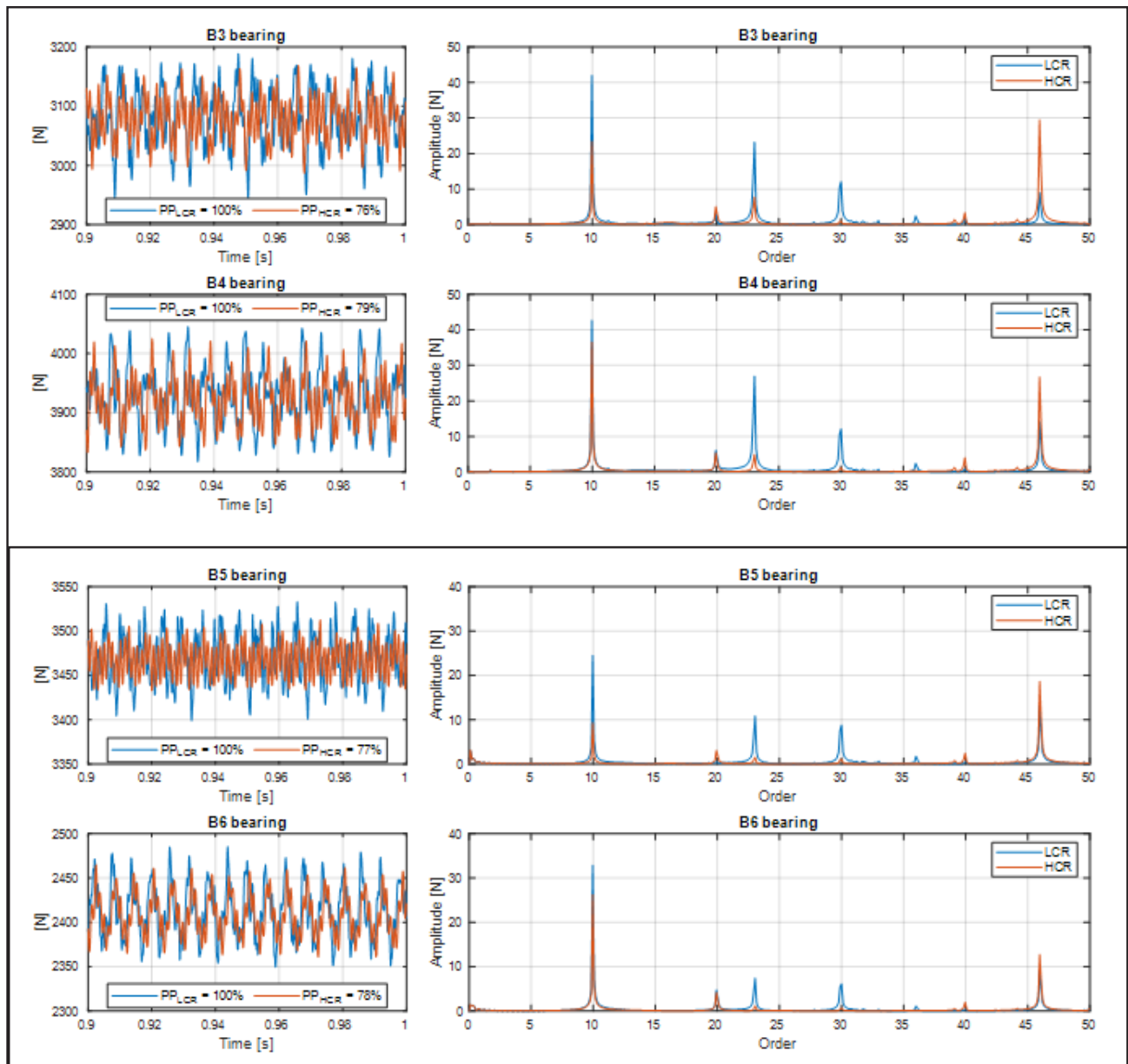


Figure 10 Bearings forces FM. (con't)

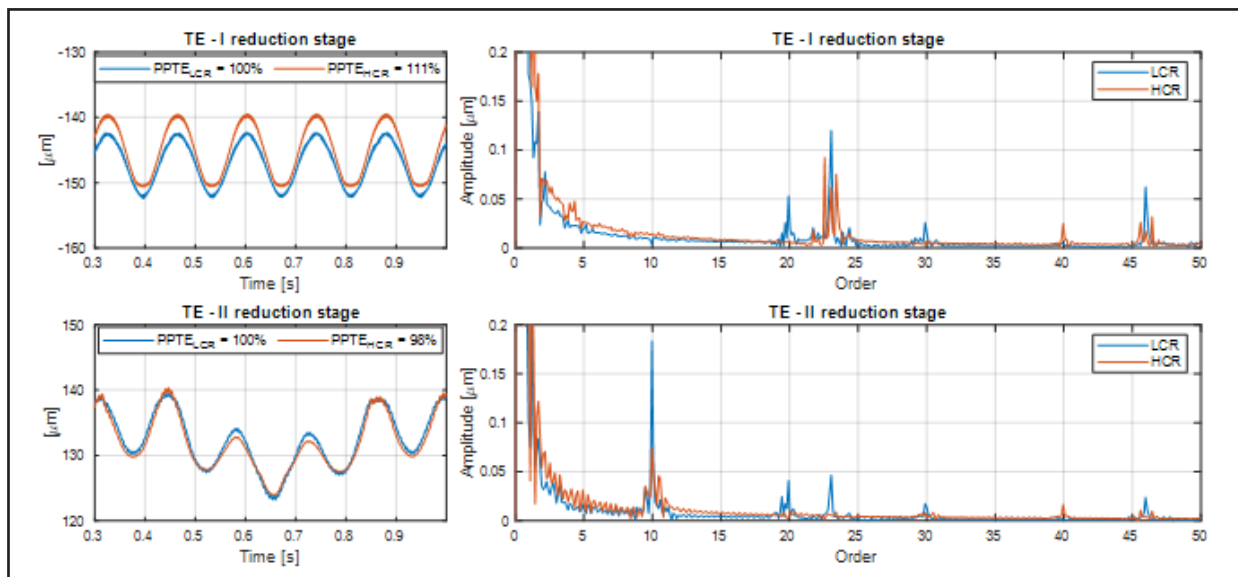


Figure 11 Transmission error and its harmonic content – flexible housing.

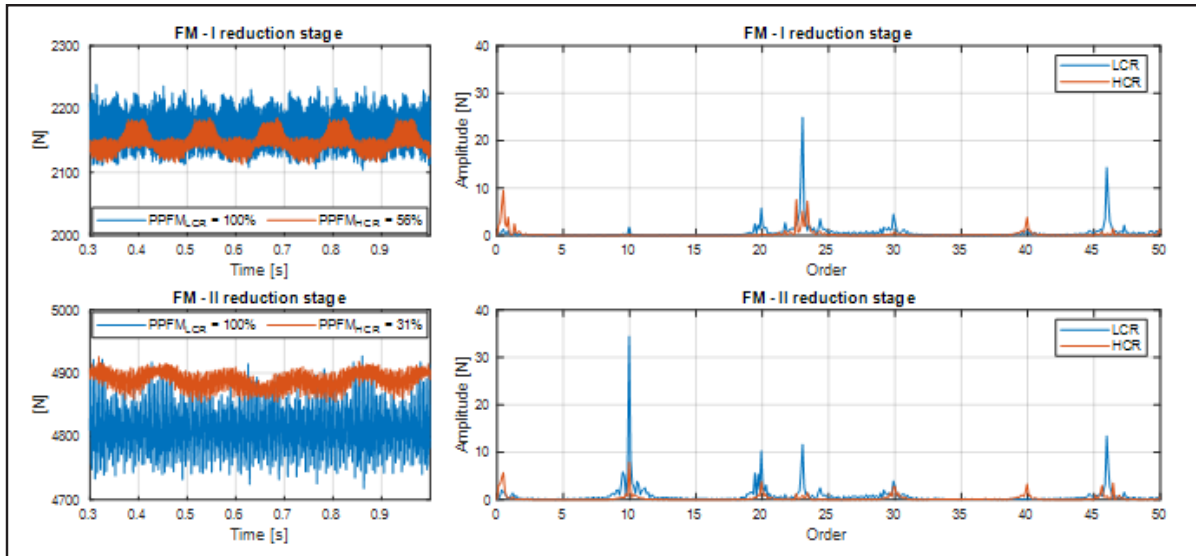


Figure 12 Gear meshing force and its harmonic content – flexible housing.

LCR gearset with the HCR gearset. For bearings B1 and B2 on the input shaft, main orders are related to the first-stage gear meshing frequency and its harmonics. For bearings B3 and B4 on the intermediate shaft, GMFs of both first- and second-stages are present. For bearings B5 and B6 on the output shaft, main orders are related to second-stage gear meshing frequency and its harmonics.

**LCR vs. HCR – flexible housing.** In the following, the results of multi-body simulation with flexible housing are shown. The transmission error is plotted (Fig. 11) for both gear stages and in both time and frequency domains. Regarding gear meshing orders, as expected, the HCR gearset has a lower TE amplitude compared to the LCR gearset. Sidebands appear because the gear meshing frequency is modulated by shaft rotational orders (as previously explained). Shaft rotational orders, calculated by means of the reduction ratios of both gear stages, are

respectively 1 for the input shaft, 0.48 for the intermediate shaft and 0.11 for the output shaft. The amplitude of the orders is remarkably similar between the LCR and HCR gearsets, since it is mainly due to the presence of misalignments and runout induced by different bearing clearances.

Gear meshing forces are shown (Fig. 12) confirming a significant reduction of the harmonic content for the HCR gearset compared to the LCR gearset.

Figure 13 shows bearing forces together with signal spectrum. The comparison among the LCR and HCR gearset shows a remarkable improvement on bearing forces, and consequently, amplitude of the signal harmonics is substantially reduced.

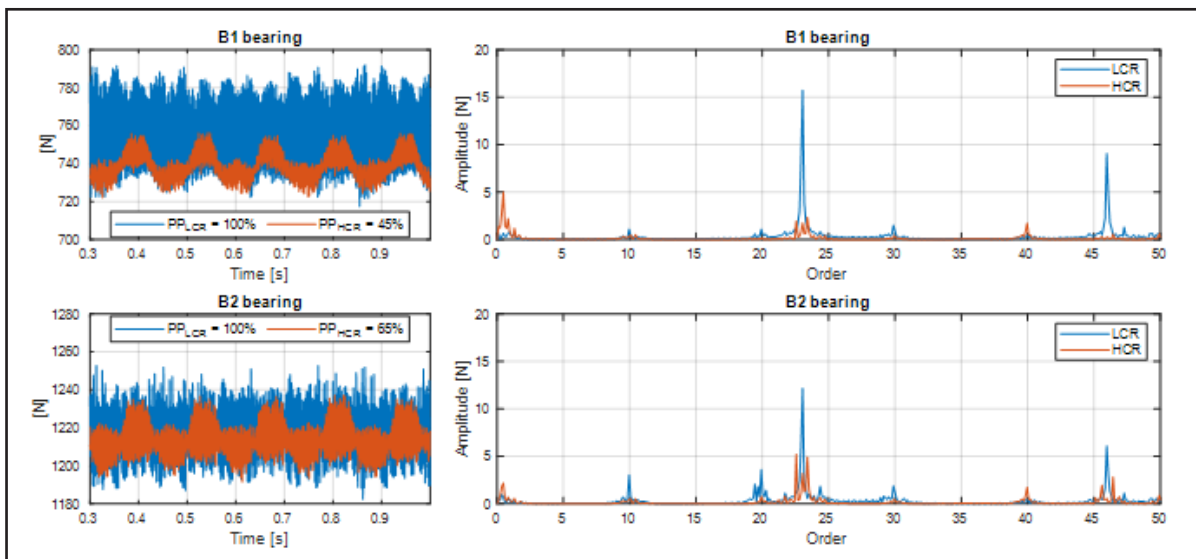


Figure 13 Bearings forces FM – flexible housing.

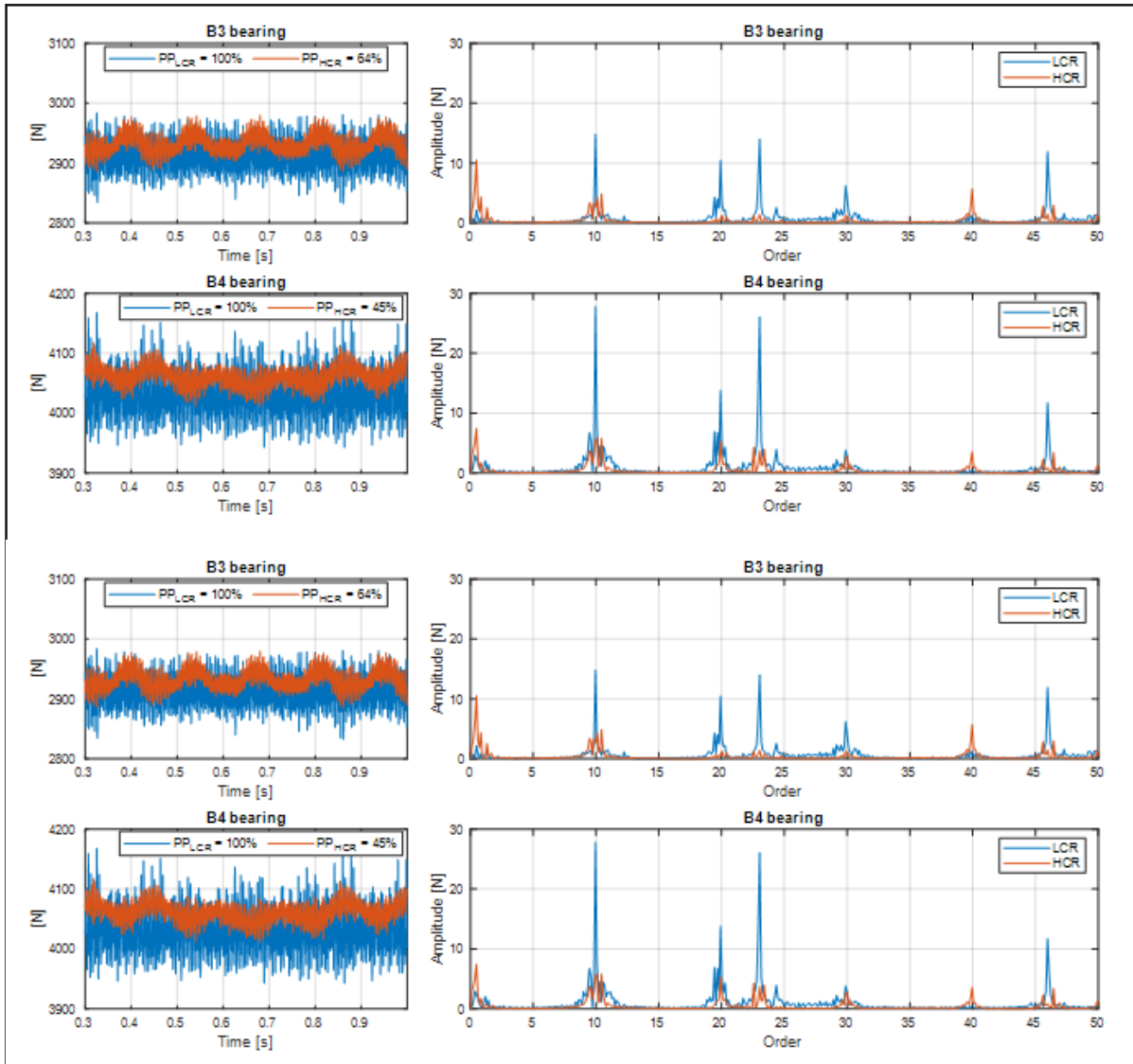


Figure 13 Bearings forces FM – flexible housing. (con't)

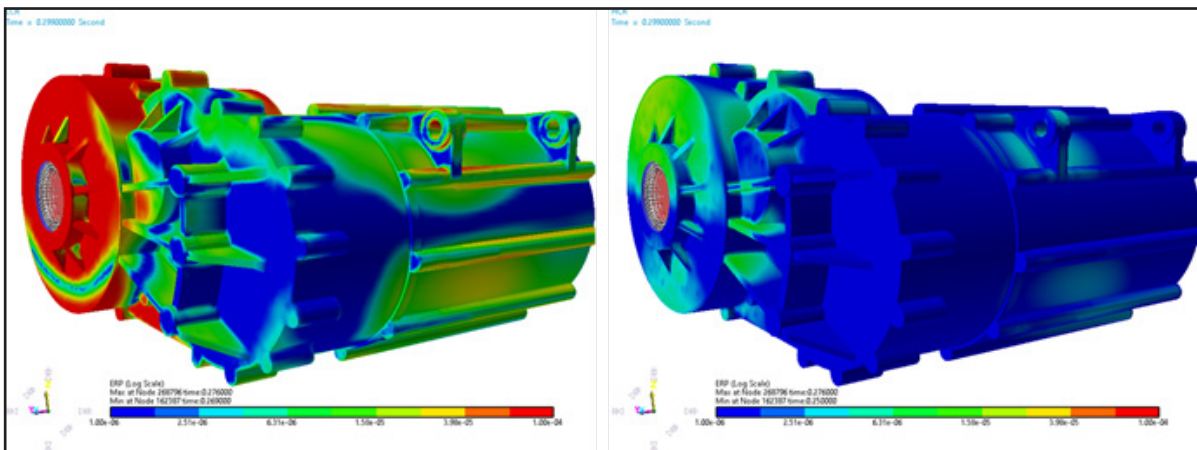


Figure 14 ERP plot comparison: LCR (left) – HCR (right).

**Housing acoustic ERP.** Acoustic equivalent radiated power (ERP) is defined as:

$$e_{ERP} = f_{RLF} \cdot \frac{1}{2} \cdot C \cdot \rho \cdot \sum (A_i \cdot v_i^2) \quad (27)$$

where  $f_{RLF}$  is the radiation loss factor,  $C$  is sound velocity,  $\rho$  is the density of a target material that transfers the vibration (i.e. — the noise) as, for example air,  $A_i$  is the area on the  $i$ -th flexible panel and  $v_i$  is the face normal velocity on the  $i$ -th flexible panel; further details can be found in (Ref. 36).

In Figure 14 the comparison among LCR gearset and HCR gearset is presented in terms of equivalent radiated power: the brighter regions are representative of a higher sound power radiation, confirming the effectiveness of adopting HCR gears for NVH improvement.

The contour plot is very helpful to understand which is the contribution of each housing panel to the overall noise emission, and to address subsequent design modifications (local stiffening of the housing, e.g. — by means of ribs).

## Conclusions

A methodology to analyze NVH performances of an automotive e-axle was addressed in the present paper. The proposed EV transmission was then designed using *KISSsys* and considering the gear microgeometry.

An extended Campbell diagram including the electrical and mechanical orders, together with the Eigenfrequencies of the constrained system, was calculated. Furthermore, the electric was modeled as a fully flexible multi-body system, and the forced response was calculated at the constant speed of the electric motor.

The NVH performance of high-contact ratio gears (HCR) was then evaluated with respect to standard ISO-53 gear profile A. Peak-to-peak transmission error (PPTE), gear meshing, and bearing forces have been compared for both configurations, showing the improvement of the HCR gears compared to the LCR gears on the NVH performance of the e-axle.

Finally, housing equivalent-radiated powers (ERP), resulting from both ISO-53 profile A and HCR gears simulations, have been compared showing the reduction of surface normal velocities. The critical areas for the design of the housing have been shown by means of contour plots.

Design improvements of the housing to minimize equivalent radiated power will be the object of further analysis. 

## For more information.

Questions or comments regarding this paper?  
Contact Davide Marano at [marano@gear-lab.it](mailto:marano@gear-lab.it).

## References

1. Continental Automotive, "Worldwide Emission Standards and Related Regulations, Passenger Cars/Light and Medium Duty Vehicles," May 2019.
2. Tousignant, T. et al. "Target Development for Transmission and Electric Motor NVH," *SAE Technical Paper*, no. 2019-01-1554, 2019.
3. Wellmann, T. et al., "NVH Aspects of Electric Drive Unit Development and Vehicle Integration," *SAE Technical Paper*, no. 2019-01-1454, 2019.
4. Smith, J.D. *Gear Noise and Vibration*, CRC Press, 2003.
5. L. L. Beranek, L.L. and L. V. Istvan. *Noise and Vibration Control Engineering - Principles and Applications*, John Wiley & Sons, Inc., 1992.
6. Åkerblom, M. "Gear Noise and Vibration: a Literature Survey," 2001.
7. Kahraman, A. and S. Rajendra. "Non-Linear Dynamics of a Spur Gear Pair," *Journal of Sound and Vibration*, Vol. 142, No. 1, pp. 49–75, 1990.
8. Inalpolat, M. and A. Kahraman. "A Dynamic Model to Predict Modulation Sidebands of Planetary Gear Set Having Manufacturing Errors," *Journal of Sound and Vibration*, Vol. 329, No. 4, pp. 371–393, 2010.

9. Özgüven, H.N. and D. R. Houser. "Dynamic Analysis of High-Speed Gears by Using Loaded Static Transmission Error," *Journal of Sound and Vibration*, Vol. 125, No. 1, pp. 71–83, 1988.
10. Özgüven, H.N. and D. R. Houser. "Mathematical Models Used in Gear Dynamics - a Review," *Journal of Sound and Vibration*, Vol. 121, No. 3, pp. 383–411, 1988.
11. Otto, M. et al. "Low Noise Gear Mesh Design for E-Mobility," *25th International Congress on Sound and Vibration, ICSV 2018*, 2018.
12. Paucker, T., M. Otto and K. Stahl. "Noise Optimization and Canceling Effects in Planetary Gear Stages Depending on Topography," *25th International Congress on Sound and Vibration, ICSV 2018*, 2018.
13. Gwinner, P., M. Otto and K. Stahl. "Vibration Behavior of High-Speed Gearings for Electrically Driven Powertrains," 2017.
14. Heider, M. et al. "Vibration Excitation of a Planetary Gear Stage," *International Conference on Gears*, 2013.
15. Barbieri, M. et al. "Dynamic Modeling of Gear Pairs," *22nd International Congress on Sound and Vibration, ICSV 2015*, 2015.
16. Bonori, G., M. Barbieri, G. Scagliarini and F. Pellicano. "Gear Vibration Reduction Using Genetic Algorithms."
17. Pellicano, F. et al. "Nonlinear Dynamics and Optimization of Spur Gears," *Nonlinear Science and Complexity*, pp. 164–179, 2007.
18. Marano, D. et al. "Modeling and Simulation of Rack-Pinion Steering Systems with Manufacturing Errors for Performance Prediction," *International Journal of Vehicle Systems Modeling and Testing*, Vol. 13, No. 2, pp. 178–198, 2018.
19. Gieras, J.F., W. Chong and C. L. Joseph. *Noise of Polyphase Electric Motors*, CRC Press, 2018.
20. Qiang, K. et al. "Test and Analysis of Electromagnetic Noise of an Electric Motor in a Pure Electric Car," *SAE Technical Paper*, No. 2019-01-1492, 2019.
21. I. 1940/1. "Mechanical Vibration-Balance Quality Requirements of Rigid Rotors," Part I: Determination of Permissible Residual Unbalance," 1998.
22. Scheffer, C. a. P. G. "Practical Machinery Vibration Analysis and Predictive Maintenance," *Elsevier*, 2004.
23. Tuma, J. *Vehicle Gearbox Noise and Vibration: Measurement, Signal Analysis, Signal Processing and Noise Reduction Measures*, John Wiley & Sons, 2014.
24. A. K. M Inalpolat. "A Theoretical and Experimental Investigation of Modulation Sidebands of Planetary Gear Sets," *Journal of Sound and Vibration*, p. 677–696, 2009.
25. ANSI/AGMA. "6123-C16," 2016.
26. SKF. "Bearing Damage and Failure Analysis."
27. Jones, R. "A Guide to the Interpretation of Vibration Frequency and Time Spectrums," *SKF-SDG-DS01*, 2011.
28. Mais, J. "Spectrum Analysis, the Key Features of Analyzing Spectra," *SKF USA Inc.*
29. J. W. C. a. L. J. Gieras. *Noise of Polyphase Electrical Motors*, CRC Press, 2006.
30. Cavalli, M., R. Lavacchielli, G. Tonelli, G. Nicoletto and E. Riva, "Comparison of Analytical and Multi-body Dynamic Approaches in the Study of a V6 Engine Piston," *Journal of Multi-Body Dynamics*, 2017.
31. He, J. and Z.-F. Fu. *Modal Analysis*, Butterworth Heinemann, 2001.
32. Jin, Y., J. Zhang and X. Guan. "Theoretical Calculation and Experimental Analysis of the Rigid Body Modes of Powertrain Mounting System," in *WSEAS Transactions on Applied and Theoretical Mechanics*, 2013.
33. van der Valk, P. "Model Reduction & Interface Modeling in Dynamic Substructuring," 2010.
34. Craig R. and M. Bampton. "Coupling of Substructures for Dynamic Analysis," *AIAA Journal*, Vol. 6, No. 7, pp. 1313–1319, 1968.
35. Kissling, U. "Layout of the Gear Micro-Geometry," 2015.
36. Functionbay. *Recurdyn V9R3 Manual*, 2020.
37. Kahraman, A. "Load Sharing Characteristics of Planetary Transmissions," *Mechanism and Machine Theory*, pp. 1151–1165, 1994.
38. Inalpolat, A.K.M. "A Dynamic Model to Predict Modulation Sidebands of a Planetary Gear Set Having Manufacturing Errors," *Journal of Sound and Vibration*, pp. 371–393, 2010.



**Davide Marano** holds a PhD in advanced mechanics from University of Modena and Reggio Emilia. He has worked as a gear engineer for ZF-TRW Automotive (Brescia-IT), and as transmission simulation specialist for Ferrari GT (Maranello-IT), focusing on gear design and optimization for NVH. He is currently a member of the Italian KISSsoft staff for training and engineering. His application focus is on NVH simulation of gearboxes for acoustic optimization and gearbox model calculation. Marano is a member of the AGMA spline committee.



**Luca Pascale** graduated in automotive engineering in 2019, with a thesis on the design of E-axles. Pascale is currently working as a simulation engineer at Ferrari S.p.A., focusing on gears optimization for strength and NVH.



**Dipl.-Ing. Jürg Langhart**, with a BS degree in mechanical engineering from HTL, Rapperswil, Switzerland, is a technical sales and project engineer in machine element and gear transmissions calculation at KISSsoft AG. Langhart is a member of the Swiss and International Standardization Organization for bevel gears (ISO TC60/WG13). Langhart has published several papers and presentations in the field of gear transmission calculation in various applications.



**Dr. Saeed Ebrahimi** is currently working in KISSsoft for developing the forced response module in power train systems. He was previously an associate professor of mechanical engineering at Yazd University in Iran. He received his PhD in mechanical engineering from Stuttgart University in Germany in 2007 and completed his post-doctoral fellowship at the Center for Intelligent Machines (CIM), McGill University, in 2008. Ebrahimi's research interests include dynamic modelling of multi-body systems, robotics, mechanisms design and vibration analysis of mechanical systems.



**Timo Giese** holds a degree in mechanical engineering at Technical University Munich (TUM). He is currently Technical Director at Function Bay Munich. Giese's research interests are focused on NVH simulation of gearboxes, dynamic simulation of machine tools and simulation of tracked vehicles.

